Preliminary design of an OWC wave energy converter battery charger

D. N. Ferreira, L. M. C. Gato, L. Zuo, and J. C. C. Henriques

Abstract—**This paper introduces a low-power off-grid oscillating water column wave energy converter with an internal battery bank. The research aims at the preliminary design and devising of the control strategy of a power electronics interface between the turbo generator and the battery bank. The converter comprises a spar buoy, a biradial turbine, a permanent magnet generator, a full-wave bridge rectifier, a braking chopper, a DC-to-DC step-down converter, and a lead-acid battery bank. The power-take-off system was modelled in Simulink/MATLAB, and its performance was assessed with steady-state simulations, considering a wave climate characteristic of Leixões, Portugal. The chamber pressure, the turbine, generator and rectifier performance were taken from experimental data sets. A simple battery model was derived from the manufacturer's datasheet. An ideal step-down DC-to-DC converter operating in discontinuous conduction mode regulates the battery charging current. This converter, in parallel with the braking chopper, adjusts the generator counter torque by regulating the current through the rectifier. Twelve system variables were recorded for selected pairs of input pressure and step-down converter design coefficient. The power at the rectifier's output terminals was mapped for the rotational speed and input pressure. The results show a system rating of 1.4 kW with 400 W of electrical power at 200 rad/s for the most frequent sea states. The range of the duty cycle, the inductance and the braking resistance were derived. Two closed-loop controllers were proposed for managing the step-down converter and the braking chopper. Their set points and saturation limits were derived from the simulation results.**

Index Terms—**off-grid power generation, wave energy, oscillating water column, biradial turbine, permanent-magnet generator**

I. Introduction

With the increasing importance of the blue economy, offshore stand-alone power systems for battery charging are emerging as potential commercial products.

A turbine driving a permanent magnet synchronous generator (PMSG) coupled to a full-wave bridge rectifier and a direct current (DC) power converter (DC-to-DC converter) is a simple implementation of an off-grid power generation system, although with lower efficiency than active rectification solutions. This configuration was extensively studied for small wind turbines [1]–[6], and to some extent, for point-absorber wave energy converters (WECs) with linear PMSGs [7], [8]. Few studies have addressed this topology applied to oscillating-water-column (OWC) WECs. A converter with a Wells turbine and a PMSG powering a DC microgrid has been studied numerically [9]. However, the self-starting capability must still be addressed since Wells turbines require a power source other than the OWC flow to reach generation speed [10], [11]. Impulse turbines may be mechanically more complex but can self-start [12], [13], making them a good option for the prime mover of power-take-off systems (PTO) with passive rectification.

This paper introduces an off-grid OWC WEC for powering offshore remote sensors and charging autonomous underwater vehicles. The WEC has an internal battery bank to store the intermittent wave power and feed it to the service loads. The research aims to establish a preliminary design for the power electronics interface between the turbo-generator and the battery bank and establish a control strategy. The main contributions of this research are the proof-of-concept for the proposed PTO to be further developed into a detailed system design and component procurement for experimental testing.

The remainder of this paper is organized as follows. Section II introduces the proposed WEC. Section III describes its numerical modelling. Section IV presents the simulation results and derives the step-down converter parameters and control laws. Section V summarizes the outcomes and outlines future research.

II. Proposed low-power off-grid OWC WEC

The proposed low-power off-grid OWC WEC comprises an OWC spar buoy, a battery-charging PTO and an internal battery bank.

A spar buoy was purposely designed for this device [14] and tank-tested at 1:10 scale for regular and irregular waves [15]. Its dimensions are given in Fig. 1.

The PTO comprises a biradial impulse turbine, a PMSG, a full-wave bridge rectifier, a capacitive filter, a DC bus with a braking chopper connected to the dump load, in parallel with a step-down converter that feeds the battery bank and service loads, see Fig. 2. The pressurized air from the OWC drives the three-phase alternate current (AC) turbo-generator, and AC-to-DC conversion is achieved with passive rectification. The rectifier output current imposes the generator counter

D. N. Ferreira (nevesferreira@tecnico.ulisboa.pt), L. M. C. Gato (luis.gato@tecnico.ulisboa.pt) and J. C. C. Henriques (joaochenriques@tecnico.ulisboa.pt) are with IDMEC, Instituto Superior Tecnico, Universidade de Lisboa, 1049-001 Lisboa, Portugal.

L. Zuo (leizuo@umich.edu) is with the Department of Naval Architecture and Marine Engineering, University of Michigan, Ann Arbor, MI 48109, USA.

This research was partially supported by the Portuguese Foundation for Science and Technology - FCT, through IDMEC, under LAETA, project UIDB/50022/2020.

Digital Object Identifier:
https://doi.org/10.36688/ewtec-2023-382

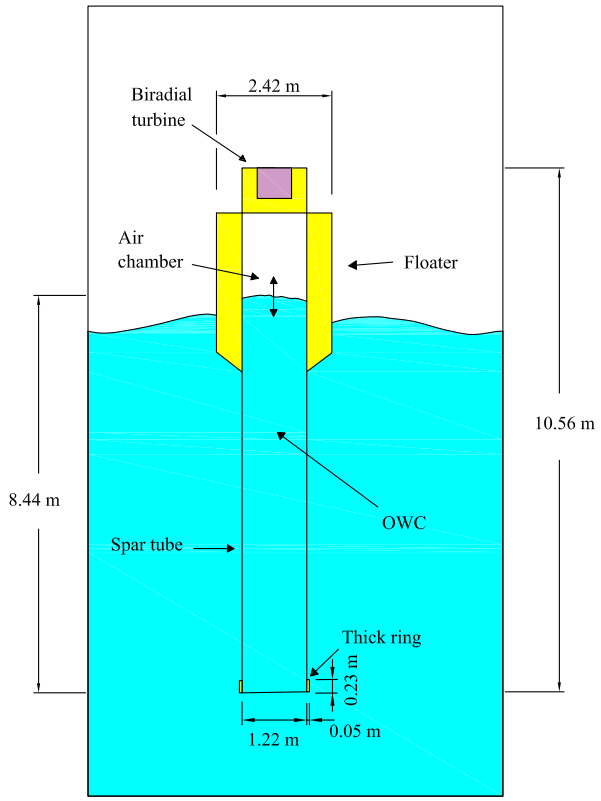

Fig. 1. Low-power OWC spar buoy dimensions [15].

torque, which is regulated by the joint action of the braking chopper and the step-down converter. The step-down converter provides power to the battery and service loads. The braking chopper supplies a dump load when the power generated exceeds the battery and service loads consumption, e.g. with fully charged batteries and no service loads. This situation presents a high risk for the PTO integrity since the turbo-generator can easily overcome its maximum rotational speed due to input pressure peaks.

III. Materials and Methods

The PTO was simulated in Simulink/MATLAB. The sub-components modelling include experimental results (OWC buoy, turbine, generator and rectifier), manufacturer data (battery) and simplified theoretical models (DC-to-DC converters). The electrical components were simulated using averaged value models, neglecting the rippling effects of transistor switching, capacitor and inductor charging/discharging.

Simulations in steady-state conditions were performed to design the converter, braking chopper, and their corresponding control laws for a specific turbine, generator, rectifier, and battery bank, considering a range of input pressure and step-down converter design coefficient.

A. OWC spar buoy

The hydrodynamic damping of an OWC equipped with an impulse turbine depends on turbine diameter and is approximately independent of its rotational speed [16]. As such, the OWC chamber relative pressure taken from experimental testing can be used as the PTO model input. The nearly quadratic damping of impulse turbines is often emulated by replacing the turbine with a calibrated round orifice on the pressure chamber wall in OWC testing [17].

The pneumatic power of an OWC device is given by

$$P_{\text{pneu}} = \frac{\dot{m}}{\rho}\Delta p\,, \tag{1}$$

where ρ is the air density Δp is the chamber relative pressure and $\dot{m}$ is the mass flow rate trough the turbine. If the turbine is replaced by a round orifice, comes

$$\dot{m} = \frac{\pi}{4} C_{\text{d}} d_{\text{o}}^2 \sqrt{2\rho} |\Delta p|^{-\frac{1}{2}} \Delta p\,, \tag{2}$$

where C_{d} is the discharge coefficient, and d_{o} is the orifice diameter. By rearranging (1) and (2), the chamber pressure can be expressed as a function of the pneumatic power and orifice properties,

$$|\Delta p| = \frac{\rho^2}{4}\left(\frac{4P_{\text{pneu}}}{\pi C_{\text{d}} d_{\text{o}}^2}\right)^{2/3}. \tag{3}$$

Equations (1), (2) and (3) are valid for instantaneous values.

The root-mean-square of the chamber pressure corresponding to each sea state was approximated by taking the associated average pneumatic power from the spar buoy power matrix and utilizing it in equation (3). The wave climate of Leixões, in the West coast of mainland Portugal, was then used to compile the pressure values into classes for which the probability of occurrence was calculated. The most relevant classes were used as the pressure input values for the PTO simulations.

B. Turbo-generator dynamics

Considering a direct rigid connection between the turbine and the generator, the rotational speed, Ω, results from the balance between the turbine torque, T_{turb}, induced by the OWC flow and the generator counter torque, T_{gen}, regulated by the joint action of the two DC-to-DC converters, Fig. 2. It is

$$J\frac{\mathrm{d}\Omega(t)}{\mathrm{d}t} = T_{\text{turb}}(t) - T_{\text{gen}}(t)\,, \tag{4}$$

where J is the total rotational inertia of the turbine and generator rotors, and t is time.

C. Biradial impulse turbine

The relationship between the turbine torque and OWC chamber pressure is taken from experimental testing results of a 30 kW fixed-guide-vane biradial turbine [18], see Fig. 3. The turbine considered for the present study is geometrically similar with a rotor diameter $D = 0.26$ m.

Neglecting effects related to Reynolds number variations, the performance of geometrically similar turbines is characterized by the pressure,

$$\Psi = \frac{\Delta p}{\rho \Omega^2 D^2}\,, \tag{5}$$

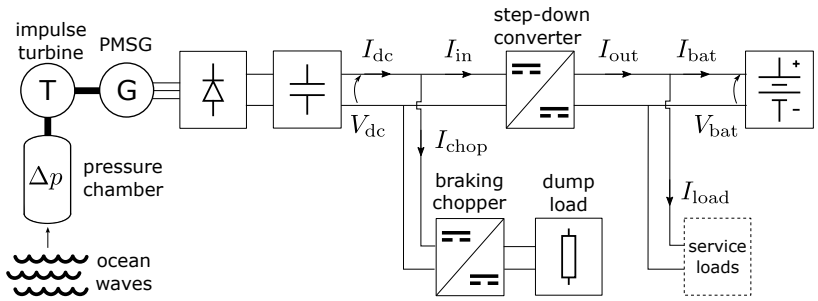

Fig. 2. Representation of an off-grid OWC battery-charger.

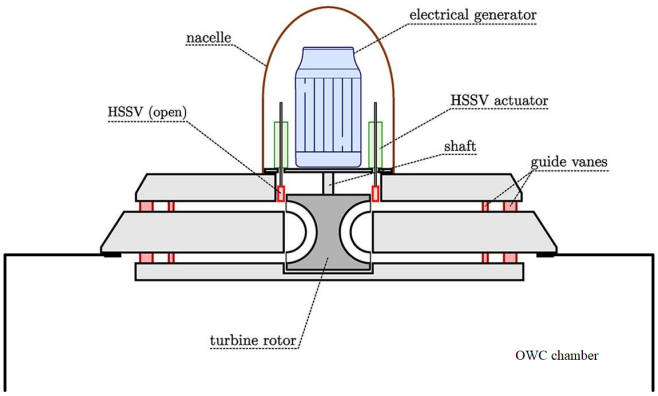

Fig. 3. Representation of a fixed-guide-vane biradial turbine.

TABLE I
GENERATOR TECHNICAL DATA [21].

Parameter	Units	Value
speed class	rpm	2000
maximum operating speed	rpm	6000
mechanically permitted speed	rpm	7200
standstill torque	Nm	6.5
standstill current	A	3.5
maximum current	A	12.2
phase inductance	mH	17.4
phase resistance (20°C)	Ohm	3.27
phase-to-phase open-circuit voltage	V/rpm	1.28
number of poles	-	8

torque (or power),

$$\Pi = \frac{T_{\text{turb}}}{\rho \Omega^2 D^5}\,, \tag{6}$$

and flow rate,

$$\Phi = \frac{Q}{\Omega D^3}\,, \tag{7}$$

coefficients, where D is the turbine rotor diameter. As such, the turbine torque is given by

$$T_{\text{turb}} = \Pi(\Psi)\rho\Omega^2 D^5\,, \tag{8}$$

The relationship between the torque coefficient, Π, and the pressure coefficient, Ψ, is approximated by the polynomial

$$\Pi(\Psi) = b_1\Psi^4 + b_2|\Psi|^3 + b_3\Psi^2 + b_4|\Psi| + b_5\,, \tag{9}$$

with $b_1 = 5.4442 \times 10^{-4}$, $b_2 = -8.3127 \times 10^{-3}$, $b_3 = 5.0681 \times 10^{-2}$, $b_3 = 9.5067 \times 10^{-1}$ and $b_4 = 9.5067 \times 10^{-1}$, for the chosen turbine geometry.

The flow rate coefficient, Φ, is related to the pressure coefficient by the fitting function

$$\Phi = \text{sign}(\Phi)\left(a_1 + a_2\sqrt{a_3\,|\Psi| + a_4}\right)\,, \tag{10}$$

with $a_1 = -6.5848 \times 10^{-2}$, $a_2 = 1.2551 \times 10^{-5}$, $a_3 = 4.6 \times 10^8$ and $a_3 = 2.7525 \times 10^7$, also valid for the chosen turbine geometry.

The turbine efficiency is derived from the other dimensionless coefficients,

$$\eta_{\text{turb}} = \frac{\Pi}{\Phi\Psi}\,. \tag{11}$$

Varying the turbine rotational speed changes the ratio between its flow rate and pressure head (turbine damping), affecting the hydrodynamic energy conversion process of OWC WECs.

It is seen in biradial impulse turbines that $K = \Psi/\Phi^2$ is approximately constant [18], [19]. Then, the relationship between pressure and flow rate for biradial turbines is given by

$$\Delta p \approx \left(\frac{\rho K}{D^4}\right) Q^2\,, \tag{12}$$

showing that the rotational speed of biradial impulse turbines has a negligible effect on the turbine damping and, as such, on the hydrodynamic energy conversion process. Note that $\Delta p(Q)$ is approximately a quadratic function, justifying the turbine emulation with a round orifice in OWC testing, see Section III-A.

D. Permanent-magnet generator and rectifier

The generator and rectifier are modelled here as a single unit, for which the relationship between the mechanical input (torque and rotational speed) and electrical output (direct current and voltage) were derived from experimental testing [20]. The generator is a SEW Eurodrive CM3C71S three-phase synchronous servomotor [21], it has a sinusoidal back electromotive force (back EMF), and a three-wire terminal interface with a star-winding configuration. The machine parameters are summarized in Table I. The rectifier is an IXYS VUO35-12NO7 standard rectifier module with a rated reverse blocking voltage of 1200 V and an output current of 35 A at 80°C.

The turbine, generator, rectifier and capacitive filter sub-asssembly were experimentally tested in steady-state conditions for a range of rotational speeds and resistive loads [20]. The relationship between the generator counter torque, T_{gen}, and the current at the

TABLE II
FITTING COEFFICIENTS FOR (14).

k	$V_{\text{dc}}/I_{\text{dc}}$ [Ohm]	$b_{1,k}$	$b_{2,k}$	r-squared
1	37	768	578	0.9984
2	44	1009	757	0.9985
3	55	1287	945	0.9991
4	73	1585	1104	0.9995
5	110	2548	1772	0.9997
6	147	2857	1922	0.9997
7	220	4015	2642	0.9997
8	330	5958	3880	0.9996
9	440	7985	5186	0.9997
10	660	11710	7525	0.9997

rectifier's output terminals, I_{dc} was found to be well fitted by [20]

$$T_{\text{gen}} = \frac{a_1 I_{\text{dc}}^* + a_2}{I_{\text{dc}}^* + a_3}\,, \tag{13}$$

where $a_1 = 26.85$, $a_2 = 3.96$, $a_3 = 17.68$. The generator phase-to-phase voltage, and hence the rectifier DC voltage, is a function of the rotational speed, Ω, with a slight influence from the electrical load $V_{\text{dc}}/I_{\text{dc}}$. The relationship

$$V_{\text{dc}_k} = \frac{b_{1,k}\Omega}{\Omega + b_{2,k}} \tag{14}$$

was established in steady-state conditions [20] with the fitting coefficients $a_{1,k}$ and $a_{2,k}$ listed in Table II for different loads with the respective coefficient of determination, r-squared.

The generator-rectifier efficiency is

$$\eta_{\text{gr}} = \frac{I_{\text{dc}} V_{\text{dc}}}{T_{\text{gen}}\Omega}\,. \tag{15}$$

E. DC-to-DC converters

The step-down DC-to-DC converter was modelled as an ideal converter. Its average output current, I_{out}, when operating in discontinuous conduction mode (DCM) between two voltage sources, V_{dc} and V_{bat}, is

$$I_{\text{out}} = \frac{d_{\text{buck}}^2}{2fL}\left(\frac{V_{\text{dc}}^2}{V_{\text{bat}}} - V_{\text{dc}}\right), \tag{16}$$

where d_{buck} is the converter switching duty cycle, f is the switching frequency and L is the converter inductance [22]. From the unitary efficiency assumption, $V_{\text{dc}} I_{\text{in}} = V_{\text{bat}} I_{\text{out}}$, comes the input current,

$$I_{\text{in}} = \frac{d_{\text{buck}}^2}{2fL}\left(V_{\text{dc}} - V_{\text{bat}}\right). \tag{17}$$

The step-down design coefficient is defined here as

$$K_{\text{buck}} = \frac{d_{\text{buck}}^2}{2fL}. \tag{18}$$

At the boundary between discontinuous and continuous conduction mode (CCM), the average output current is

$$I_{\text{out}_{\text{lim}}} = \frac{d_{\text{buck}}}{2fL}\left(V_{\text{dc}} - V_{\text{bat}}\right). \tag{19}$$

As such, Eqs. (16) and (17) are valid only if $I_{\text{out}} < I_{\text{out}_{\text{lim}}}$ [22].

The braking chopper is modelled here as an ideal switch in series with a resistor. The current through the braking resistor is

$$I_{\text{chop}} = \frac{d_{\text{chop}}}{R} V_{\text{dc}}\,, \tag{20}$$

where d_{chop} is the chopper switching duty cycle and R is the braking resistance.

Note that the joint action of the DC-to-DC converters regulates the generator counter torque as seen by Eq. (13) and Fig. 2,

$$I_{\text{dc}} = I_{\text{in}} + I_{\text{chop}}\,, \tag{21}$$

and that the step-down converter regulates the current to the battery and loads,

$$I_{\text{out}} = I_{\text{bat}} + I_{\text{load}}\,. \tag{22}$$

F. Battery bank

The battery bank comprises four series-connected Mastervolt gel batteries model MVG 12/85 [23] rated at 12 V with a nominal capacity of $C_{20} = 85$ Ah at 25°C for a current $I_{20} = 4.25$ A. Gel batteries are often used as service batteries in off-grid systems such as recreational vehicles. They tend to be more expensive than absorbent glass mat (AGM) batteries which are commonly used to power starter motors. Gel batteries tend to have lower discharge but higher charge currents than AGM. Charging follows the DIN 41773 Standard, also known as IUoU or three-step charging. The charge parameters presented here are tuned for the battery model and connection chosen.

The first step is the bulk phase, also called the constant-current phase, and it starts when the bank voltage drops below 47.6 V ($V_{\text{blk}} = 47.6$ V). The bank current should be set between 20 and 25.5 A. The upper limit is 42.5 A at the cost of reducing the batteries' useful life. The bulk phase ends when the bank voltage reaches 57 V. This voltage can be adjusted as a function of the batteries' temperature to extend their useful life. The bank should not be loaded at this stage.

The second step is the absorption phase or constant-voltage boost stage. The bank should be in over-voltage at $V_{\text{abs}} = 57$ V while its current decreases. The absorption phase continues until 6% of the maximum charging current is reached. For the selected bank, it is 1.5 A.

The third step is the float phase. The bank voltage should be kept at $V_{\text{flt}} = 55.2$ V while the bank current can vary between the maximum charge and discharge currents imposed by the state-of-charge and existing service loads. If the bank voltage drops below $V_{\text{blk}} = 47.6$ V, the service load supply should be interrupted, and the charger should return to the bulk phase.

G. Control

In the absence of the breaking chopper, a closed control loop regulates the battery charging and keeps the turbo-generator current below a set threshold. Depending on the charging stages, the process variable

is either the battery bank current or voltage (see Section III-F). The manipulated variable is the step-down converter output current, I_{out}, defined in Eq. (16). The error between the set-point, for each charging stage according to Section III-F, and the process variables is fed to the controller whose output signal is the step-down converter duty cycle, d_{buck}. The service load is the disturbance on the charging process, as it will consume part of the step-down converter output current. If the service load is larger than the output current, the battery discharges, otherwise, it charges. Consider Eqs. (13), (16), (17), (21) and (22), and assume $I_{\text{chop}} = 0$ and $I_{\text{load}} = 0$. It is seen that the battery I_{bat}, and rectifier, I_{dc}, currents increase with the converter's duty cycle d_{buck}. As such, the generator counter torque becomes entirely dependent on the battery charging process, with a high battery charging current resulting in a high counter torque. An upper saturation limit on the duty cycle becomes necessary to keep the generator counter torque and the battery charging current under their allowable values. This limit was derived from the simulations and is presented in Section IV.

A separate closed control loop indirectly keeps the turbo-generator rotational speed below its limit by guaranteeing a minimum rectifier output current, and consequently, a minimum counter torque. Consider Eqs. (13), (16), (17), (21) and (22), but assume $I_{\text{bat}} = 0$ and $I_{\text{load}} = 0$. It is seen that if the step-down converter output current is $I_{\text{out}} = 0$, there is no generator counter torque because $I_{\text{dc}} = 0$ unless $I_{\text{chop}} \neq 0$. The braking chopper creates this current by connecting the braking resistor to the DC bus. Here the process variable is the rectifier output current, I_{dc}, and the manipulated variable is the braking chopper current, I_{chop}. The error between the set-point, which is a minimum rectifier output current, $I_{\text{dc}_{\text{min}}}$, and the process variable is fed into a controller whose output signal is the braking chopper duty cycle, d_{chop}. It is seen from Eqs. (20) and (21) that while $I_{\text{in}} > I_{\text{dc}_{\text{min}}}$, it is $d_{\text{chop}} = 0$, otherwise $0 < d_{\text{chop}} < 1$. Then it becomes necessary to define an adequate braking resistance, R, that guarantees the minimum rectifier output current for the expected range of voltages, V_{dc}. The minimum current and braking resistance were derived from the simulations and are presented in Section IV.

H. Simulation setup

Simulations in steady-state conditions were performed for a range of OWC chamber pressures, Δp, and step-down converter design coefficients, $K_{\text{buck}} = d_{\text{buck}}^2/(2fL)$.

The Simulink model is illustrated in Fig. 4 and is described as follows. Note that the description and illustration of the block's input/output ports were simplified for clarity. Other ports and blocks were used, namely for variable measurement and recording. The battery bank was modelled as a constant voltage source, where $V_{\text{bat}} = V_{\text{float}} = 55.2\,\text{V}$, connected in series with a resistor that models the battery bank internal resistance, $R_{\text{bat}} = 2.48 \times 10^{-4}\,\text{Ohm}$. Custom function blocks defined the turbine, generator and rectifier

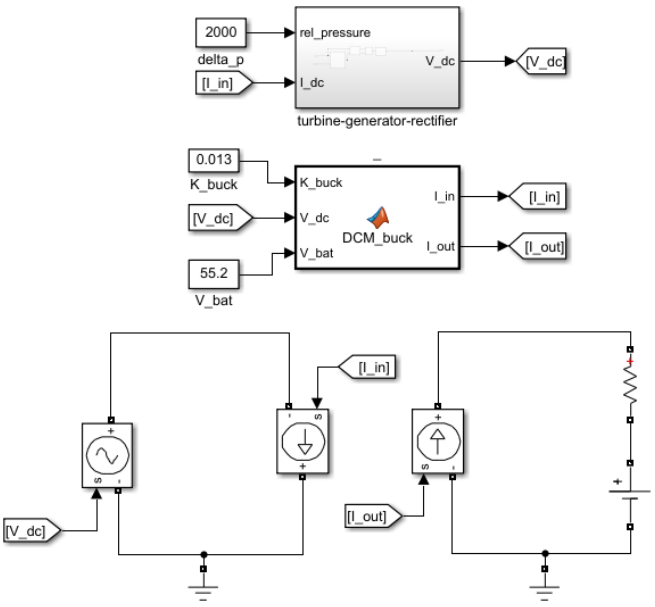

Fig. 4. MATLAB/Simulink model (simplified).

equations. These components were then inserted in a sub-assembly block with the chamber pressure, Δp, and rectifier output current, I_{dc}, as inputs and the rectifier output voltage, V_{dc}, as output. The step-down converter was modelled with a custom function block using the design coefficient, K_{buck}, the rectifier output voltage, V_{dc} and the battery voltage, V_{bat} as inputs, and the converter's input and output currents as the block's output, I_{in} and I_{out}, respectively. It was not necessary to simulate the braking chopper and the service loads in the scope of this study. Making $I_{\text{load}} = 0$ and $I_{\text{chop}} = 0$, it comes $I_{\text{dc}} = I_{\text{in}}$ and $I_{\text{bat}} = I_{\text{out}}$. The turbine-generator-rectifier, the step-down converter, and the battery blocks were connected with a Simscape Specialized Power Systems grid.

Twelve variables were recorded in addition to the two inputs, Δp and K_{buck}: turbine dimensionless coefficients, Ψ, Φ, Π and η_{turb}, flowrate, Q, rotational speed, Ω, turbine and generator torque, T_{turb} and T_{gen}, rectifier output voltage and current, V_{dc} and I_{dc}, generator-rectifier efficiency, η_{gr}, and battery current, I_{bat}. Note that since $I_{\text{chop}} = I_{\text{load}} = 0$, it is $I_{\text{dc}} = I_{\text{in}}$ and $I_{\text{bat}} = I_{\text{out}}$.

IV. Results

The probability distribution, ϕ, of the OWC spar buoy pneumatic chamber root-mean-square pressure, rms(Δp), for a discharge coefficient $C_{\text{d}} = 0.683$, orifice diameter $d_{\text{o}} = 0.16\,\text{m}$ and considering a deployment site off the West coast of mainland Portugal [15] is illustrated in Fig. 5. It is seen that 30% of the sea states for this location result in a root-mean-square pressure between $1\,\text{kPa}$ and $1.5\,\text{kPa}$. In 65% of the time, the pressure is $0.5 < \text{rms}(\Delta p) < 2.0\,\text{kPa}$. These results were used to define the pressure ranges for the simulations in steady-state conditions.

The characterization study was performed for six OWC chamber pressures in the range $0.5 < \Delta p < 5.0\,\text{kPa}$ and eleven step-down converter design coefficient in the range

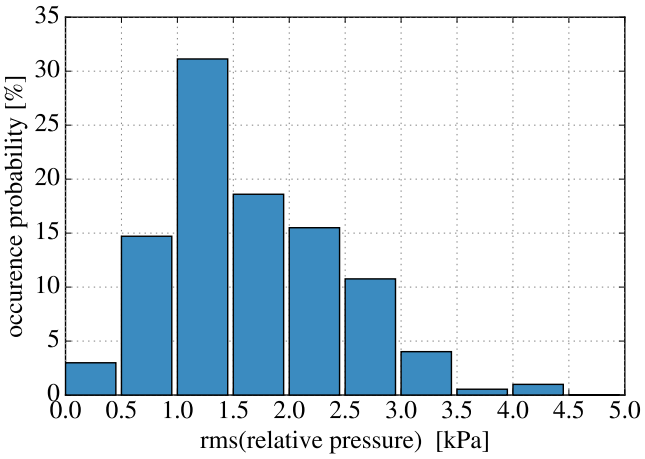

Fig. 5. Probability distribution of the OWC chamber rms pressure.

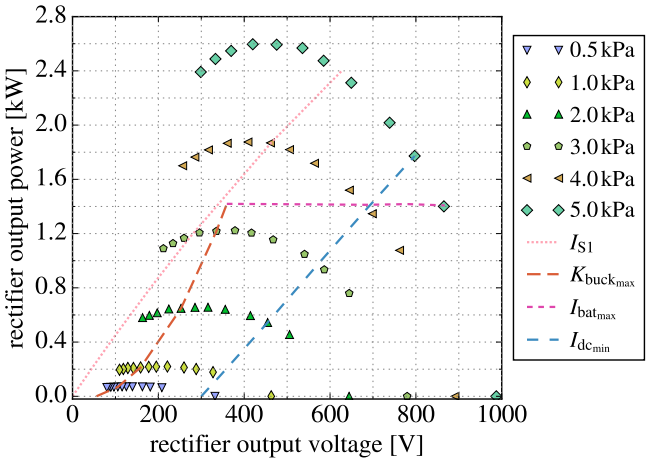

Fig. 6. Relationship between rectifier output power, $P_{dc} = I_{dc}V_{dc}$, and voltage, V_{dc}, for: a range of input pressures, Δp, generator current limit, I_{S1}, converter design coefficient $K_{buck_{max}} = 0.013\,\text{Ohm}^{-1}$, maximum battery bank charging power, $I_{bat} = 25.5\,\text{A}$, and the established minimum rectifier output current, $I_{dc_{min}}$.

$0 < K_{buck} < 33 \times 10^{-3}\,\text{Ohm}^{-1}$, in a total of seventy-two $(\Delta p, K_{buck})$ pairs. Every simulation ran until steady-state was achieved for all recorded variables. The results were compiled into two charts for sizing the step-down converter, the braking chopper and defining the control laws. Fig. 6 relates the rectifier output power, P_{dc}, and voltage, V_{dc}, and Fig. 7 relates it with the turbo-generator rotational speed, Ω. The points sets labelled $0.5\,\text{kPa}$ to $5\,\text{kPa}$ result from the characterization study by varying K_{buck} while keeping the chamber pressure, Δp equal to the respective label value. The remaining lines are related to achieve specific operational conditions relevant for system design.

The horizontal line labelled $I_{bat_{max}}$ illustrates the rectifier output power for the maximum battery charging current under the assumption of an ideal step-down converter. Naturally, some variation to the shape and location of this curve is expected with more advanced modelling. Still, it is a practical first approach for defining the converter rated power.

The line labelled $K_{buck_{des}}$ illustrates the power for constant step-down converter design coefficient, $K_{buck} = 0.013\,\text{Ohm}^{-1}$. This value was chosen for the

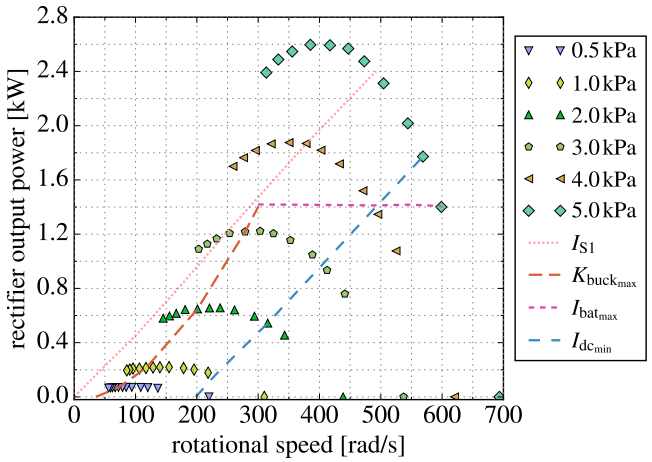

Fig. 7. Relationship between rectifier output power, $P_{dc} = I_{dc}V_{dc}$, and turbo-generator rotational speed, Ω, for: a range of input pressures, Δp, generator current limit, I_{S1}, converter design coefficient $K_{buck_{max}} = 0.013\,\text{Ohm}^{-1}$, maximum battery bank charging power, $I_{bat} = 25.5\,\text{A}$, and the established minimum rectifier output current, $I_{dc_{min}}$.

design because the line intersects the maximum battery charging current curve, $I_{bat_{max}}$, closely below the generator current limit, I_{S1} curve, and approximately follows the maximum power points. Recalling the transition between DCM and CCM, Eq. (19) can be rewritten to provide the duty cycle,

$$d_{buck} = \frac{K_{buck}}{I_{out_{lim}}}\left(V_{dc} - V_{bat}\right). \tag{23}$$

An output current at the transition point of $I_{out_{lim}} = 28\,\text{A}$ was chosen for precaution. Simulation results reveal that a converter with $K_{buck} = K_{buck_{des}} = 0.013\,\text{Ohm}^{-1}$ achieves this current at $\Delta p = 3.35$ kPa with a rectifier voltage of $V_{dc} = 378\,\text{V}$. As such, from Eq. (23), the converter maximum duty cycle is $d_{buck} = 0.15$. A frequency $f = 30\,\text{kHz}$ was assumed based on the conventional power transistor modules, micro-controllers and gate drivers available in the market. Then, from the definition of the converter design coefficient, $K_{buck} = d_{buck}^2/(2fL)$, comes its inductance $L = 29\,\mu\text{H}$.

As discussed in Sec. III-G, the duty cycle range, d_{buck}, should be limited to avoid generator and battery over-currents. Fig. 7 shows that limiting the converter duty cycle to $d_{buck} = 0.15$ keeps the generator-rectifier and battery currents below their respective rated values if the speed is $\Omega < 300\,\text{rad/s}$. Above this value, the battery charging current is the limiting factor for the maximum duty cycle. So, a limit as a function of the rotational speed was defined for the controller. From the simulations results represented by the line labelled $I_{bat_{max}}$, the relationship between the duty cycle and rotational speed is plotted in Fig. 8. An analytical function was fitted to the data on Fig. 8 with a coefficient of determination of R-squared $= 0.9982$ resulting in the following control law for the maximum allowable duty

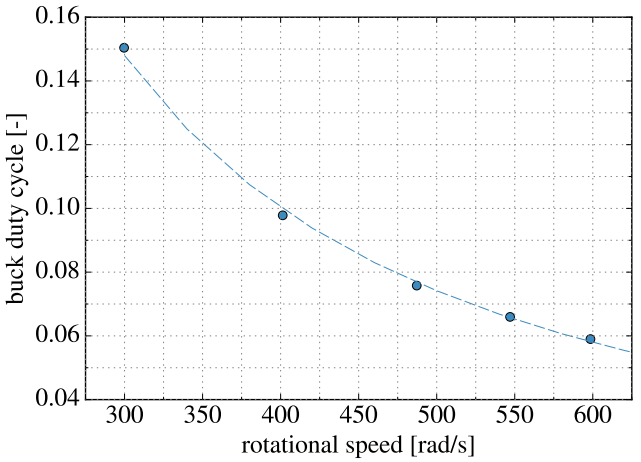

Fig. 8. Relationship between step-down converter duty cycle, d_{buck}, and rotational speed, Ω, for a battery charging current $I_{\text{bat}} = I_{\text{bat}_{\text{max}}} = 25.5\,\text{A}$.

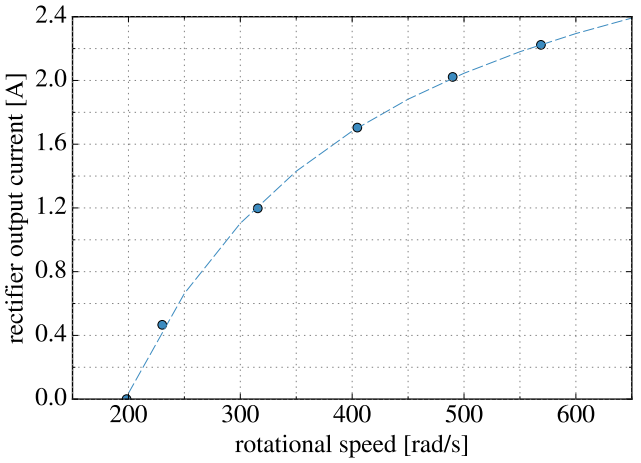

Fig. 9. Relationship between the rectifier output current, I_{dc}, and the generator rotational speed, Ω, for the prescribed minimum rectifier output power.

cycle,

$$d_{\text{buck}_{\text{max}}}(\Omega)[-] = \begin{cases} 0.15 & , 0 \leq \Omega \leq 300\,\text{rad/s} \\ 330.51\Omega^{-1.352} & , \Omega > 300\,\text{rad/s}\,. \end{cases} \tag{24}$$

The minimum rectifier output current was derived by prescribing a linear variation of the rectifier output power between $P_{\text{dc}} = 0$ at $V_{\text{dc}} = 300\,\text{V}$ and $P_{\text{dc}} = 1.78\,\text{kW}$ at $V_{\text{dc}} = 800\,\text{V}$, as represented in Figs. 6 and 7 by the line labelled $I_{\text{dc}_{\text{min}}}$. The resulting minimum current is $I_{\text{dc}_{\text{min}}} = 3.56 - 1069/V_{\text{dc}}$. Recalling the braking chopper current definition of Eq. (20) comes

$$R = d_{\text{chop}} \left(\frac{3.56}{V_{\text{dc}}} - \frac{1069}{V_{\text{dc}}^2} \right)^{-1}. \tag{25}$$

Considering that $0 \leq d_{\text{chop}} \leq 1$, the allowable resistance range is $0 \leq R \leq 337.4\,\text{Ohm}$, if neglecting negative values of R. A resistance value of $R = 220\,\text{Ohm}$ was selected, resulting in a chopper duty cycle in the range $0 \leq d_{\text{chop}} \leq 0.65$. The relationship between the rectifier output current, $I_{\text{dc}} = I_{\text{dc}_{\text{min}}}$, and the turbo-generator rotational speed, Ω is illustrated in Fig. 9 and was fitted with the function

$$I_{\text{dc}_{\text{min}}}(\Omega)[\text{A}] = \begin{cases} 0 & , 0 \leq \Omega \leq 200\,\text{rad/s} \\ \dfrac{3.632\Omega - 717.7}{\Omega + 36.99} & , \Omega > 200\,\text{rad/s}\,, \end{cases} \tag{26}$$

with a coefficient of determination R-squared $= 0.9995$. This function provides the chopper controller with the set-points to guarantee a minimum current at the rectifier output terminals.

V. Conclusion

This paper introduced an off-grid oscillating-water-column wave energy converter with an internal battery bank for powering remote sensing equipment and autonomous underwater vehicles. The research aimed at the preliminary design and devising the control strategy of a simple power electronics interface for charging the converter's internal battery bank.

From existing experimental data on the pre-set mechanical components, battery bank and deployment site, a topology was devised consisting of a DC-to-DC step-down converter, operating in discontinuous conduction mode in parallel with a braking chopper and two closed-loop controllers.

The DC-to-DC converter duty cycle range, frequency and inductance were calculated for part procurement. A control strategy for this converter was established to avoid generator and battery over-current. The braking resistance, braking chopper duty cycle range needed to limit the rotational speed of the turbo-generator in the absence of battery or service loads was found.

A first approach on the converter-rated electrical power was found to be $1.4\,\text{kW}$ at $300\,\text{rad/s}$ with $400\,\text{W}$ of electrical power expected during the most frequent sea-states at $200\,\text{rad/s}$. The rated power was derived under the assumption of an ideal DC-to-DC converter and should be updated with more comprehensive modelling.

The simulation setup can be easily adapted to run with prescribed electrical components, and new simulations should be performed based on market availability. The methodology can also be directly employed for different deployment sites, buoys, turbines and generators to assess their impact on the required electrical components.

Finally, after implementing the closed-loop controllers, the simulation setup can be easily adapted to run with time-dependent inputs, namely input pressure time series, service loads, and varying duty cycles.

References

[1] K. Lo, Y. Chen, and Y. Chang, "MPPT battery charger for stand-alone wind power system," *IEEE Transactions on Power Electronics*, vol. 26, no. 6, pp. 1631–1638, 2011.

[2] C. N. Bhende, S. Mishra, and S. G. Malla, "Permanent magnet synchronous generator-based standalone wind energy supply system," *IEEE Transactions on Sustainable Energy*, vol. 2, no. 4, pp. 361–373, 2011.

[3] M. E. Haque, K. M. Muttaqi, and M. Negnevitsky, "Control of a stand alone variable speed wind turbine with a permanent magnet synchronous generator," in *IEEE Power and Energy Society General Meeting - Conversion and Delivery of Electrical Energy in the 21st Century*, 2008, pp. 1–9.

[4] N. Mendis, K. M. Muttaqi, and S. Perera, "Management of battery-supercapacitor hybrid energy storage and synchronous condenser for isolated operation of PMSG based variable-speed wind turbine generating systems," *IEEE Transactions on Smart Grid*, vol. 5, no. 2, pp. 944–953, 2014.

[5] J. C. Y. Hui, A. Bakhshai, and P. K. Jain, "An energy management scheme with power limit capability and an adaptive maximum power point tracking for small standalone PMSG wind energy systems," *IEEE Transactions on Power Electronics*, vol. 31, no. 7, pp. 4861–4875, 2016.

[6] S. Malla and C. Bhende, "Voltage control of stand-alone wind and solar energy system," *International Journal of Electrical Power & Energy Systems*, vol. 56, pp. 361–373, 2014.

[7] R. Ekström, B. Ekergard, and M. Leijon, "Electrical damping of linear generators for wave energy converters – A review," *Renewable and Sustainable Energy Reviews*, vol. 42, pp. 116–128, 2015.

[8] L. Wang, M. Lin, E. Tedeschi, J. E. om, and J. Isberg, "Improving electric power generation of a standalone wave energy converter via optimal electric load control," *Energy*, vol. 211, p. 118945, 2020.

[9] S. Seo, J. Kim, E. Muljadi, R. M. Nelms, and H. Moeljanto, "Holistic design of small-scale oscillating water column in stand-alone DC microgrid," in *IEEE Energy Conversion Congress and Exposition (ECCE)*, 2022, pp. 1–8.

[10] S. Raghunathan, "The Wells air turbine for wave energy conversion," *Progress in Aerospace Sciences*, vol. 31, no. 4, pp. 335–386, 1995.

[11] D. O'Sullivan, J. Griffiths, M. G. Egan, and A. W. Lewis, "Development of an electrical power take off system for a sea-test scaled offshore wave energy device," *Renewable Energy*, vol. 36, no. 4, pp. 1236–1244, 2011.

[12] Y. Cui, Z. Liu, X. Zhang, C. Xu, H. Shi, and K. Kim, "Self-starting analysis of an OWC axial impulse turbine in constant flows: Experimental and numerical studies," *Applied Ocean Research*, vol. 82, pp. 458–469, 2019.

[13] A. F. O. F. ao, L. M. C. Gato, and E. P. A. S. Nunes, "A novel radial self-rectifying air turbine for use in wave energy converters. Part 2. Results from model testing," *Renewable Energy*, vol. 53, pp. 159–164, 2013.

[14] J. C. C. Henriques, J. C. C. Portillo, L. M. C. Gato, R. P. F. Gomes, D. N. Ferreira, and A. F. O. F. ao, "Design of oscillating-water-column wave energy converters with an application to self-powered sensor buoys," *Energy*, vol. 112, pp. 852–867, 10 2016.

[15] C. L. G. Oikonomou, R. P. F. Gomes, and L. M. C. Gato, "Unveiling the potential of using a spar-buoy oscillating-water-column wave energy converter for low-power stand-alone applications," *Applied Energy*, vol. 292, p. 116835, 6 2021.

[16] L. M. C. Gato, J. C. C. Henriques, and A. A. D. Carrelhas, "Sea trial results of the biradial and Wells turbines at Mutriku wave power plant," *Energy Conversion and Management*, vol. 268, p. 115936, 2022.

[17] J. C. C. Portillo, J. C. C. Henriques, L. M. C. Gato, and A. F. O. F. ao, "Model tests on a floating coaxial-duct OWC wave energy converter with focus on the spring-like air compressibility effect," *Energy*, vol. 263, p. 125549, 2023.

[18] A. A. D. Carrelhas, L. M. C. Gato, J. C. C. Henriques, A. F. O. F. ao, and J. Varandas, "Test results of a 30 kW self-rectifying biradial air turbine-generator prototype," *Renewable and Sustainable Energy Reviews*, vol. 109, pp. 187–198, 7 2019.

[19] A. A. D. Carrelhas, L. M. C. Gato, J. C. C. Henriques, and A. F. O. F. ao, "Experimental study of a self-rectifying biradial air turbine with fixed guide-vanes arranged into two concentric annular rows," *Energy*, vol. 198, p. 117211, 2020.

[20] D. N. Ferreira, L. M. C. Gato, and J. C. C. Henriques, "Testing of a permanent magnet synchronous generator for off-grid OWC wave energy converters," Internal Report, 2023, IDMEC, Instituto Superior Tecnico.

[21] *CM3C63 - CM3C100 Synchronous Servomotors*, https://download.sew-eurodrive.com/download/pdf/29194652.pdf, SEW Eurodrive, 2020, accessed on May 2023.

[22] N. Mohan, T. M. Undeland, and W. P. Robbins, *Power Electronics. Converters, Applications and Design*, 3rd ed. John Wiley and Sons, Inc, 2003.

[23] "Mastervolt MVG 12/85," https://www.mastervolt.com/products/mvg-12v-gel/mvg-12-85-gel/, accessed on May 2023.